Published in final edited form as:

*IEEE Trans Med Imaging*. 2017 February ; 36(2): 467–477. doi:10.1109/TMI.2016.2614967.

# Optimizing MR Scan Design for Model-Based $T_1$, $T_2$ Estimation from Steady-State Sequences

**Gopal Nataraj [Student Member, IEEE]**,
Department of Electrical Engineering and Computer Science, University of Michigan, Ann Arbor, MI, USA

**Jon-Fredrik Nielsen**, and
Department of Biomedical Engineering, University of Michigan, Ann Arbor, MI, USA

**Jeffrey A. Fessler [Fellow, IEEE]**
Department of Electrical Engineering and Computer Science, University of Michigan, Ann Arbor, MI, USA

## Abstract

Rapid, reliable quantification of MR relaxation parameters $T_1$ and $T_2$ is desirable for many clinical applications. Steady-state sequences such as Spoiled Gradient-Recalled Echo (SPGR) and Dual-Echo Steady-State (DESS) are fast and well-suited for relaxometry because the signals they produce are quite sensitive to $T_1$ and $T_2$ variation. However, $T_1$, $T_2$ estimation with these sequences typically requires multiple scans with varied sets of acquisition parameters. This paper describes a systematic framework for selecting scan types (*e.g.*, combinations of SPGR and DESS scans) and optimizing their respective parameters (*e.g.*, flip angles and repetition times). The method is based on a Cramér-Rao Bound (CRB)-inspired min-max optimization that finds scan parameter combinations that robustly enable precise object parameter estimation. We apply this technique to optimize combinations of SPGR and DESS scans for $T_1$, $T_2$ relaxometry in white matter (WM) and grey matter (GM) regions of the human brain at 3T field strength. Phantom accuracy experiments show that SPGR/DESS scan combinations are in excellent agreement with reference measurements. Phantom precision experiments show that trends in $T_1$, $T_2$ pooled sample standard deviations reflect CRB-based predictions. *In vivo* experiments show that in WM and GM, $T_1$ and $T_2$ estimates from a pair of optimized DESS scans exhibit precision (but not necessarily accuracy) comparable to that of optimized combinations of SPGR and DESS scans. To our knowledge, $T_1$ maps from DESS acquisitions alone are new. This example application illustrates that scan optimization may help reveal new parameter mapping techniques from combinations of established pulse sequences.

### Index Terms

$T_1$, $T_2$ relaxometry; optimal experimental design; Cramér-Rao Bound; magnetic resonance imaging

Correspondence to: Gopal Nataraj.

Color versions of one or more of the figures in this paper are available online at http://ieeexplore.ieee.org.

## I. Introduction

Fast, accurate quantification of spin-lattice and spin-spin relaxation parameters $T_1$ and $T_2$ has been of longstanding interest in MRI. Many researchers have suggested that $T_1$, $T_2$ maps may serve as biomarkers for monitoring the progression of various disorders [1]. Neurological applications include: lesion classification in multiple sclerosis [2]; tumor characterization [3, 4]; and symptom onset prediction in stroke [5, 6]. In addition, $T_1$, $T_2$ have shown promise for detecting hip and knee cartilage degeneration [7, 8] and for assessing cardiac dysfunction due to iron overload [9] or edema [10]. Motivated by this broad interest in $T_1$, $T_2$ mapping, this paper describes a systematic method to guide MR scan design.

Classical pulse sequences such as inversion/saturation recovery (IR/SR) or (single) spin echo (SE) yield relatively simple methods for $T_1$ or $T_2$ estimation, respectively; however, these methods require several scans, each with long repetition time $T_R$, leading to undesirably long acquisitions. Numerous modifications such as the Look-Locker method [11], multi-SE trains [12], or fast **k**-space trajectories [13–15] have been proposed to accelerate $T_1$ [16–19] and $T_2$ [20–23] relaxometry with these classical sequences. These techniques are more sensitive to model non-idealities [24–26], and are still speed-limited by the long $T_R$ required for (near)-complete $T_1$ recovery.

Steady-state (SS) pulse sequences [27, 28] permit short $T_R$, and are thus inherently much faster than classical counterparts. SS techniques are well-suited for relaxometry because the signals produced are highly sensitive to $T_1$ and $T_2$ variation. However, short $T_R$ times also cause SS signals to be complex functions of both desired and undesired (*nuisance*) parameters, complicating quantification. Furthermore, some such methods [29, 30] still require scan repetition, though individual scans are now considerably shorter. Despite these difficulties, the potential for rapid scanning with high $T_1$, $T_2$ sensitivity has motivated numerous SS relaxometry studies [29–38].

The dual-echo steady-state (DESS) sequence [39] was recently proposed as a promising SS imaging technique for $T_2$ estimation [35]. Because it produces two distinct signals per excitation, the DESS sequence can reduce scan repetition requirements by recording twice as much data per scan. As with other SS methods, the resulting signals [40, 41] are complicated functions of $T_1$, $T_2$, and other parameters. Prior works have isolated $T_2$ dependencies using either algebraic manipulations of the first- and second-echo signals [35, 36] or separate scans to first estimate nuisance parameters [42]. Although DESS concurrently encodes rich $T_1$ and $T_2$ information, these methods have shied away from using DESS for $T_1$ estimation, either through bias-inducing approximations, or noise-propagating sequential estimation, respectively.

Whether it be with DESS, other sequences, or even combinations thereof, it is generally unclear how to best assemble a *scan profile* (*i.e.*, a collection of scans) for a fixed amount of scan time. Furthermore, for a given scan profile, it is typically not obvious how to best select acquisition parameters (*e.g.*, flip angles, repetition times, etc.) for relaxometry. In this paper,

the term *scan design* refers to the related problems of scan profile selection and scan parameter optimization.

Historically, scan design for relaxometry has predominantly been explored using figures of merit related to estimator precision. In particular, several studies have used the Cramér-Rao Bound (CRB), a statistical measure that bounds the minimum variance of an unbiased estimator. Earlier works have used the CRB and variations to select inversion times for recovery experiments [43, 44], flip angles for spoiled gradient-recalled echo (SPGR) sequences [45], and echo times for SE experiments [46]. More recent studies have considered additional scan design challenges, including scan time constraints [47], multiple latent parameters [48], multiple scan parameter types [49], and latent parameter spatial variation [50, 51].

The aforementioned studies consider scan parameter optimization for profiles consisting of *only one* pulse sequence. In contrast, this paper introduces a general framework for robust, application-specific scan design for parameter estimation from *combinations* of pulse sequences. The framework first finds multiple sets of scan parameters that achieve precise estimation within a tight, *application-specific* range of object parameters (*e.g.*, $T_1$, $T_2$, etc.). The framework then chooses the one scan parameter set most *robust* to estimator precision degradation over a broader range of object parameters. As a detailed example, we optimize three combinations of DESS and SPGR sequences for $T_1$, $T_2$ mapping. For a fixed total scan time, we find that well-chosen DESS scans alone can be used to estimate both $T_1$ and $T_2$ with precision and robustness comparable to combinations of DESS and SPGR. This example illustrates that, with careful scan profile design, well-established pulse sequences can find use in new estimation problems.

This paper is organized as follows. Section II uses a general signal model to describe a CRB-inspired min-max optimization problem for robust, application-specific scan optimization. Section III adapts the DESS signal models to our framework and optimizes three practical DESS/SPGR combinations to show that, even in the presence of radiofrequency (RF) field inhomogeneity, DESS is a promising option for $T_1$, $T_2$ relaxometry. Section IV describes simulation, phantom, and *in vivo* experiments and discusses corresponding results. Section V discusses practical challenges and suggests future directions. Section VI summarizes key contributions.

## II. A CRB-Inspired Scan Selection Method

### A. A Generalized Signal Model

A broad class of MR pulse sequences useful for parameter mapping produce, after reconstruction, a set of noisy images $y_d(\cdot)$ that can be described with the following general model:

$$y_d(\mathbf{r}) = f_d(\mathbf{x}(\mathbf{r}); \boldsymbol{\nu}(\mathbf{r}), \mathbf{p}_d) + \varepsilon_d(\mathbf{r}),\ d = 1, \ldots, D, \quad (1)$$

where $\mathbf{x}(\mathbf{r}) \in \mathbb{C}^L$ collects $L$ *latent* object parameters, at position $\mathbf{r}$; $\boldsymbol{\nu}(\mathbf{r}) \in \mathbb{C}^K$ gathers $K$ *known* object parameters at $\mathbf{r}$; $\mathbf{p}_d \in \mathbb{R}^P$ denotes a set of $P$ scan parameters chosen for the $d$th dataset; $f_d : \mathbb{C}^L \times \mathbb{C}^K \times \mathbb{R}^P \mapsto \mathbb{C}$ is a (pulse-sequence dependent) function that models the noiseless signal obtained from the $d$th dataset; and $\varepsilon_d \sim \mathbb{C}\mathcal{N}(0, \sigma_d^2)$ is assumed, for sake of simplicity, to be independent, complex Gaussian noise[1] [54, 55]. (As a concrete example, for $T_2(\cdot)$ mapping from single SE datasets, $\mathbf{x}(\cdot)$ could collect spin density and $T_2(\cdot)$; $\boldsymbol{\nu}(\cdot)$ could collect known off-resonance and RF field inhomogeneities; and $\mathbf{p}_d$ could assign the $d$th echo time, chosen to yield image $y_d(\cdot)$.)

A scan profile consists of $D$ datasets from a combination of pulse sequences. Let $\mathbf{y}(\mathbf{r}) := [y_1(\mathbf{r}), \ldots, y_D(\mathbf{r})]^\top \in \mathbb{C}^D$ collect the noisy signals at $\mathbf{r}$ from all datasets, $\mathbf{P} := [\mathbf{p}_1, \ldots, \mathbf{p}_D] \in \mathbb{R}^{P \times D}$ gather the corresponding scan parameters, and vector function $\mathbf{f} : \mathbb{C}^L \times \mathbb{C}^K \times \mathbb{R}^{P \times D} \mapsto \mathbb{C}^D$ naturally extend scalar function $f$, where $(\cdot)^\top$ denotes vector transpose. Then the log-likelihood function is (to within a constant independent of $\mathbf{x}(\mathbf{r})$):

$$\ln L(\mathbf{x}(\mathbf{r})) = -\frac{1}{2} \| \mathbf{y}(\mathbf{r}) - \mathbf{f}(\mathbf{x}(\mathbf{r}); \boldsymbol{\nu}(\mathbf{r}), \mathbf{P}) \|^2_{\sum^{-1/2}}, \quad (2)$$

where covariance matrix $\sum := \operatorname{diag}\left(\sigma_1^2, \ldots, \sigma_D^2\right)$ is diagonal due to the assumption of independence between scans.

Under suitable regularity conditions[2], the Fisher information matrix $\mathbf{I}(\mathbf{x}(\mathbf{r}); \boldsymbol{\nu}(\mathbf{r}), \mathbf{P}) \in \mathbb{C}^{L \times L}$ [56] is a measure useful for characterizing the precision of unbiased estimates of $\mathbf{x}(\mathbf{r})$ from $\mathbf{y}(\mathbf{r})$, given $\boldsymbol{\nu}(\mathbf{r})$ and $\mathbf{P}$:

$$\begin{aligned} \mathbf{I}(\mathbf{x}(\mathbf{r}); \boldsymbol{\nu}(\mathbf{r}), \mathbf{P}) &:= \left( [\nabla_{\mathbf{x}} \ln L(\mathbf{x}(\mathbf{r}))]^\dagger [\nabla_{\mathbf{x}} \ln L(\mathbf{x}(\mathbf{r}))] \right) \\ &= [\nabla_{\mathbf{x}} \mathbf{f}(\mathbf{x}(\mathbf{r}); \boldsymbol{\nu}(\mathbf{r}), \mathbf{P})]^\dagger \sum^{-1} [\nabla_{\mathbf{x}} \mathbf{f}(\mathbf{x}(\mathbf{r}); \boldsymbol{\nu}(\mathbf{r}), \mathbf{P})], \end{aligned} \quad (3)$$

where $\mathbb{E}(\cdot)$ denotes expectation; $\nabla_{\mathbf{x}}$ denotes a row gradient with respect to $\mathbf{x}$ at fixed $\mathbf{r}$; and $(\cdot)^\dagger$ denotes Hermitian transpose. In particular, the matrix Cramér-Rao Bound (CRB) [57] ensures that any unbiased estimator $\hat{\mathbf{x}}(\mathbf{r})$ satisfies

$$\operatorname{cov}(\hat{\mathbf{x}}(\mathbf{r}); \boldsymbol{\nu}(\mathbf{r}), \mathbf{P}) \succeq \mathbf{I}^{-1}(\mathbf{x}(\mathbf{r}); \boldsymbol{\nu}(\mathbf{r}), \mathbf{P}), \quad (4)$$

[1] Though the noise distribution of **k**-space raw data is usually well-modeled as complex white Gaussian, the noise distribution of the $d$th reconstructed image $y_d(\cdot)$ depends both on the acquisition and reconstruction. If single receive channel **k**-space data is fully-sampled on a Cartesian grid, each dataset $y_d(\cdot)$ is recoverable via separate Fourier transform, and is thus complex Gaussian and independent across datasets. However, if **k**-space data is multi-channel, undersampled, and/or non-Cartesian, it may be preferable that $y_d(\cdot)$ be estimated by more sophisticated techniques, *e.g.*, [52, 53]. In such cases, reconstructed image noise is unlikely to be Gaussian-distributed.

[2] In particular, **f** must be analytic in complex components of **x** at each **r**.

where for arbitrary, equally sized matrices **A** and **B**, matrix inequality **A** ≥ **B** means **A** − **B** is positive semi-definite. In the following, we design an optimization problem based on the CRB to guide MR scan design for relaxometry.

### B. Min-max Optimization Problem for Scan Design

Following [58], we focus on minimizing a weighted average of the variances in each of the $L$ latent object parameter estimates. A reasonable objective function for overall estimator precision is therefore given by

$$\Psi(\mathbf{x}(\mathbf{r});\boldsymbol{\nu}(\mathbf{r}),\mathbf{P})=\mathrm{tr}\,(\mathbf{W}\mathbf{I}^{-1}(\mathbf{x}(\mathbf{r});\boldsymbol{\nu}(\mathbf{r}),\mathbf{P})\mathbf{W}^{\perp}), \quad (5)$$

where $\mathbf{W}\in\mathbb{R}^{L\times L}$ is a diagonal, application-specific matrix of weights, preselected to control the relative importance of precisely estimating the $L$ latent object parameters; and tr (·) denotes the matrix trace operation. For scan design, we would like to minimize (5) with respect to scan parameters **P**.

The CRB depends not only on **P** but also on the spatially varying object parameters **x**(·) and $\boldsymbol{\nu}(\cdot)$. Thus, one cannot perform scan design by "simply" minimizing $\Psi$ over the scan parameters **P**. Instead, we pose a practical and application-dependent *min-max* optimization problem for scan design: we seek candidate scan parameters $\breve{\mathbf{P}}$ over a search space $\mathscr{P}$ that *minimize* the worst-case, *i.e.*, *maximum* cost $\tilde{\Psi}^{\mathrm{t}}$, as viewed over "tight" parameter ranges $\mathscr{X}_{\mathrm{t}}$ and $\mathscr{N}_{\mathrm{t}}$:

$$\breve{\mathbf{P}}\in\underset{\mathbf{P}\in\mathscr{P}}{\arg\min}\,\tilde{\Psi}^{\mathrm{t}}(\mathbf{P}), \quad \text{where} \quad (6)$$

$$\tilde{\Psi}^{\mathrm{t}}(\mathbf{P})=\max_{\substack{\mathbf{x}\in\mathscr{X}_{\mathrm{t}}\\ \boldsymbol{\nu}\in\mathscr{N}_{\mathrm{t}}}}\Psi(\mathbf{x};\boldsymbol{\nu},\mathbf{P}). \quad (7)$$

Here, we select *latent* object parameter set $\mathscr{X}_{\mathrm{t}}$ based on the application and *known* parameter set $\mathscr{N}_{\mathrm{t}}$ based on the spatial variation typically observed in the known parameters $\boldsymbol{\nu}(\cdot)$. Min-max approach (6) should ensure good estimation precision over a range of parameter values.

Since $\Psi$ is in general non-convex with respect to **P**, it may have multiple global minimizers as well as other scan parameters that are nearly global minimizers. To improve robustness to object parameter variations, we form an expanded set of candidate scan parameters by also including scan parameters that yield costs to within a tolerance $\delta\ll 1$ of the optimum. Mathematically, we define this expanded set of candidate scan parameter combinations (for a given scan profile) as

$$\mathscr{S} := \left\{ \mathbf{P} : \tilde{\Psi}^{\mathrm{t}}(\mathbf{P}) - \tilde{\Psi}^{\mathrm{t}}(\breve{\mathbf{P}}) \leq \delta \tilde{\Psi}^{\mathrm{t}}(\breve{\mathbf{P}}) \right\}. \quad (8)$$

To select amongst these candidate scan parameters, we employ a robustness criterion: we select the single scan parameter $\mathbf{P}^*$ that degrades the least when the worst-case cost is viewed over widened object parameter sets $\mathscr{X}_{\mathrm{b}} \supseteq \mathscr{X}_{\mathrm{t}}$ and $\mathscr{N}_{\mathrm{b}} \supseteq \mathscr{N}_{\mathrm{t}}$:

$$\mathbf{P}^* = \arg\min_{\mathbf{P} \in \mathscr{S}} \tilde{\Psi}^{\mathrm{b}}(\mathbf{P}), \quad \text{where} \quad (9)$$

$$\tilde{\Psi}^{\mathrm{b}}(\mathbf{P}) = \max_{\substack{\mathbf{x} \in \mathscr{X}_{\mathrm{b}} \\ \boldsymbol{\nu} \in \mathscr{N}_{\mathrm{b}}}} \Psi(\mathbf{x}; \boldsymbol{\nu}, \mathbf{P}). \quad (10)$$

To compare different scan profiles, we select corresponding search spaces $\mathscr{P}$ to satisfy acquisition constraints (*e.g.*, total scan time), but otherwise hold optimization parameters $\mathbf{W}$, $\delta$, $\mathscr{X}_{\mathrm{t,b}}$, and $\mathscr{N}_{\mathrm{t,b}}$ fixed. Since $\Psi$ is data-independent, we can solve (6) and (9) offline for each scan profile. The result of each profile's min-max optimization process (9) is a corresponding optimized scan parameter matrix $\mathbf{P}^*$ that is suitable for the range of latent $\mathbf{x}$ and known $\boldsymbol{\nu}$ object parameters specified in $\mathscr{X}_{\mathrm{t}}$ and $\mathscr{N}_{\mathrm{t}}$, and is robust to variations in those parameters over broader sets $\mathscr{X}_{\mathrm{b}}$ and $\mathscr{N}_{\mathrm{b}}$, respectively.

## III. Application: Optimizing SS Sequences for $T_1$, $T_2$ Relaxometry in the Brain

This section applies the methods of Section II.B to the problem of scan design for joint $T_1$, $T_2$ estimation from combinations of SS sequences. Section III.A presents a brief overview of the DESS signals, formulating models to permit estimation of as few nuisance parameters as possible. Section III.B details how we use optimization problems (6) and (9) to tailor three combinations of DESS and SPGR scans for precise $T_1$, $T_2$ estimation in white matter (WM) and grey matter (GM) regions of the human brain. Section III.C compares the predicted performance of the three optimized scan profiles.

### A. The DESS Signal Model

The DESS sequence interlaces RF excitations with unbalanced spoiler gradients of fixed area [39] to produce two distinct signals per excitation. If the gradient lobe area is carefully chosen to dominate through-voxel field inhomogeneity gradients, yet not introduce significant diffusive effects [59–61], the bulk steady-state signal $s_{\mathrm{D}}$ (from a voxel centered at position $\mathbf{r}$) immediately *before* ($t \approx 0^-$) and *after* ($t \approx 0^+$) an RF excitation centered at time $t = 0$ can be written as

$$s_{\mathrm{D}}(\mathbf{r},0^{-})=-iM_0(\mathbf{r})\tan\frac{\alpha(\mathbf{r})}{2}\,[1-\eta(\mathbf{r},T_{\mathrm{R}})] \quad \text{and} \tag{11}$$

$$s_{\mathrm{D}}(\mathbf{r},0^{+})=+iM_0(\mathbf{r})\tan\frac{\alpha(\mathbf{r})}{2}\,\left[1-\frac{\eta(\mathbf{r},T_{\mathrm{R}})}{\xi(\mathbf{r},T_{\mathrm{R}})}\right];\text{where} \tag{12}$$

$$\eta(\mathbf{r},t):=\sqrt{\frac{1-E_2^2(\mathbf{r},t)}{1-E_2^2(\mathbf{r},t)/\xi^2(\mathbf{r},t)}}, \quad \text{and} \tag{13}$$

$$\xi(\mathbf{r},t):=\frac{1-E_1(\mathbf{r},t)\cos\alpha(\mathbf{r})}{E_1(\mathbf{r},t)-\cos\alpha(\mathbf{r})}. \tag{14}$$

Here, $E_u(\mathbf{r}, t) := \exp(-t/T_u(\mathbf{r}))$ for $u \in \{1, 2\}$ describes longitudinal or transverse relaxation at time $t$, respectively; $M_0(\mathbf{r}) \in \mathbb{C}$ is proportional to spin density; flip angle $\alpha(\mathbf{r}) = \alpha_0 \kappa(\mathbf{r})$ is decomposed as a nominal (prescribed) value $\alpha_0$ with spatial variation $\kappa(\mathbf{r}) \approx 1$ due to RF field inhomogeneities; $T_{\mathrm{R}}$ is repetition time; and $i := \sqrt{-1}$. Signal models (11) and (12) neglect relaxation and off-resonance effects during each (short) RF pulse[3], and assume RF rotations about the $\hat{x}$-axis.

We model each voxel's macroscopic broadening distribution to be Cauchy $(\bar{\omega}(\mathbf{r}), R_2'(\mathbf{r}))$, where $\bar{\omega}(\mathbf{r})$ denotes median off-resonance frequency and $R_2'(\mathbf{r})$ is the broadening bandwidth. If we time readout gradients to form echoes symmetrically centered at echo time $T_{\mathrm{E}}$ before and after RF excitation, then the noiseless DESS signals are well approximated as

$$s_{\mathrm{D}}(\mathbf{r},-T_{\mathrm{E}}) \approx s_{\mathrm{D}}(\mathbf{r},0^{-})\,E_2^{-1}(\mathbf{r},T_{\mathrm{E}})\,e^{-\left(R_2'(\mathbf{r})+i\bar{\omega}(\mathbf{r})\right)T_{\mathrm{E}}} \tag{15}$$

$$s_{\mathrm{D}}(\mathbf{r},+T_{\mathrm{E}}) \approx s_{\mathrm{D}}(\mathbf{r},0^{+})\,E_2(\mathbf{r},T_{\mathrm{E}})\,e^{-\left(R_2'(\mathbf{r})-i\bar{\omega}(\mathbf{r})\right)T_{\mathrm{E}}}. \tag{16}$$

[3]Finite-duration RF effects influence SS signals more strongly for shorter $T_{\mathrm{R}}$, larger $\alpha_0$, and smaller $T_2/T_1$ [62]. In this work, RF pulse durations do not exceed 11% of repetition times and do not excite nominal flip angles greater than 35°. Phantom results (*cf.* Fig. 1) show that for these scan parameters, the influence of finite-duration RF effects on $T_1$, $T_2$ estimates is small even for $T_2/T_1 \approx 0.1$ as in WM/GM.

In (15) and (16), nuisance parameters $M_0(\mathbf{r})$, $R_2'(\mathbf{r})$, $\kappa(\mathbf{r})$, and $\bar{\omega}(\mathbf{r})$ complicate estimation of $T_1(\mathbf{r})$ and $T_2(\mathbf{r})$. For simplicity, we take $\kappa(\mathbf{r})$ to be known from a separately acquired RF transmit field $B_1^+(\mathbf{r})$ scan. To avoid (separate or joint) $\bar{\omega}(\mathbf{r})$ estimation, we choose to use magnitude DESS data, at the expense of slight model mismatch (studied with simulations in Section IV.A) in (1) due to Rician noise. By fixing $T_E$ across acquisitions and defining

$$M_E(\mathbf{r}) := M_0(\mathbf{r}) E_2(\mathbf{r}, T_E) e^{-R_2'(\mathbf{r}) T_E}, \quad (17)$$

we can rewrite magnitude signals as functions of $L = 3$ latent and $K = 1$ known object parameters, collected as $\mathbf{x}(\mathbf{r}) := [M_E(\mathbf{r}), T_1(\mathbf{r}), T_2(\mathbf{r})]^\top$ and $\nu(\mathbf{r}) := \kappa(\mathbf{r})$, respectively:

$$f_1(\mathbf{x}(\mathbf{r}); \nu(\mathbf{r}), \mathbf{p}) := |s_D(\mathbf{r}, -T_E)| = M_E(\mathbf{r}) \tan\frac{\alpha(\mathbf{r})}{2} E_2^{-2}(\mathbf{r}, T_E) [1 - \eta(\mathbf{r}, T_R)] \quad (18)$$

$$f_2(\mathbf{x}(\mathbf{r}); \nu(\mathbf{r}), \mathbf{p}) := |s_D(\mathbf{r}, +T_E)| = M_E(\mathbf{r}) \tan\frac{\alpha(\mathbf{r})}{2} \left[1 - \frac{\eta(\mathbf{r}, T_R)}{\xi(\mathbf{r}, T_R)}\right]; \quad (19)$$

where $\mathbf{p} := [\alpha_0, T_R]^\top$ collects the $P = 2$ scan parameters we are free to optimize. From here, we use the scan design method described in Section II to select an optimized $\mathbf{p}$ corresponding to each DESS scan within a particular scan profile.

## B. Scan Design Details

There are numerous candidate scan profiles involving DESS and/or other pulse sequences that may be useful for fast, accurate $T_1$, $T_2$ mapping. In this work, we consider combinations of DESS and SPGR scans [63]. With proper RF phase cycling and gradient spoiling, the SPGR signal $s_S$ can be expressed without any explicit $T_2(\mathbf{r})$ dependence:

$$s_S(\mathbf{r}, T_E) = \frac{i M_E(\mathbf{r}) \sin\alpha(\mathbf{r}) (1 - E_1(\mathbf{r}, T_R))}{1 - E_1(\mathbf{r}, T_R)\cos\alpha(\mathbf{r})}. \quad (20)$$

SPGR's reduced dependence on spatially varying unknowns is reason for its use for $T_1$ mapping [30–32] and subsequent $T_2$ mapping from other sequences [29, 42]. In a similar spirit, we examine scan profiles containing SPGR over other SS sequences because we predict that the SPGR sequence's $T_2$-independence may help estimators disentangle $T_2$ from other unknown sources of DESS signal contrast.

As written in (20), each SPGR scan also leaves $\mathbf{p} = [\alpha_0, T_R]^\top$ as $P = 2$ scan parameters available to optimize. A given scan profile consisting of $C_{SPGR}$ SPGR and $C_{DESS}$ DESS scans yields $D = C_{SPGR} + 2C_{DESS}$ datasets. We optimize such a scan profile by solving (9) over a dimension-$PD = 2(C_{SPGR} + 2C_{DESS})$ space of scan parameters.

We select constraints on search space $\mathcal{P}$ based on hardware limitations and desired scan profile properties. Since each pair of DESS signals must share the same choice of **p**, the search space is reduced to $\mathcal{A}_{0,\mathrm{SPGR}}^{C_{\mathrm{SPGR}}} \times \mathcal{A}_{0,\mathrm{DESS}}^{C_{\mathrm{DESS}}} \times \mathcal{T}_{\mathrm{R,SPGR}}^{C_{\mathrm{SPGR}}} \times \mathcal{T}_{\mathrm{R,DESS}}^{C_{\mathrm{DESS}}}$ (superscripts denote Cartesian powers). We assign flip angle ranges $\mathcal{A}_{0,\mathrm{SPGR}} = \mathcal{A}_{0,\mathrm{DESS}} \leftarrow [5, 90]°$ to restrict RF energy deposition. We set feasible $T_{\mathrm{R}}$ solution sets $\mathcal{T}_{\mathrm{R,SPGR}} \leftarrow [12.2,+\infty)$ms and $\mathcal{T}_{\mathrm{R,DESS}} \leftarrow [17.5,+\infty)$ms based on pulse sequence designs that control for other scan parameters. These control parameters are described in further detail in Section IV, and are held fixed in all subsequent SPGR and DESS experiments. To equitably compare optima from different scan profiles, we require $\mathbf{T}_{\mathrm{R}} := [T_{\mathrm{R},1},\ldots, T_{\mathrm{R},C_{\mathrm{SPGR}}}, T_{\mathrm{R},C_{\mathrm{SPGR}}+1},\ldots, T_{\mathrm{R},C_{\mathrm{SPGR}}+C_{\mathrm{DESS}}}]^{\top}$ to satisfy a total time constraint, $\|\mathbf{T}_{\mathrm{R}}\|_1 \leq T_{\mathrm{R,max}}$. For a scan profile consisting of $C_{\mathrm{SPGR}}$ SPGR and $C_{\mathrm{DESS}}$ DESS scans, these constraints collectively reduce the search space dimension from $PD$ to $2(C_{\mathrm{SPGR}} + C_{\mathrm{DESS}}) - 1$.

Prior works have considered $T_1$ or $T_2$ estimation from as few as 2 SPGR [29, 45] or 1 DESS [35] scan(s), respectively. We likewise elect to optimize the $(C_{\mathrm{SPGR}}, C_{\mathrm{DESS}}) \leftarrow (2, 1)$ scan profile as a benchmark. We choose $T_{R,\mathrm{max}} \leftarrow 2(12.2)+ 1(17.5) = 41.9$ms and select other scan profiles capable of meeting this time constraint. Requiring that candidate profiles contain $C_{\mathrm{DESS}} \geq 1$ DESS scans for $T_2$ contrast and satisfy $D \geq L(= 3)$ for well-conditioned estimation, we note that (1, 1) and (0, 2) are the only other eligible profiles.

In the ensuing experiments, we focus on precise $T_1$, $T_2$ estimation in the brain and design latent object parameter ranges $\mathcal{X}_{\mathrm{t}} = \mathcal{M}_{\mathrm{E,t}} \times \mathcal{T}_{1,\mathrm{t}} \times \mathcal{T}_{2,\mathrm{t}}$ and $\mathcal{N}_{\mathrm{t}} = \mathcal{K}_{\mathrm{t}}$ accordingly. Noting that $T_1 \sim 10\,T_2$, we choose $\mathbf{W} \leftarrow \mathrm{diag}\,(0, 0.1, 1)$ in (5) to place roughly equal importance on precise $T_1$ vs. $T_2$ estimation. Since **W** places zero weight on $M_{\mathrm{E}}$ estimation (obviating the need for complex differentiation in (3)), it is easily shown that $\Psi$ depends on $M_{\mathrm{E}}$ only through a constant scale factor; thus it suffices to consider $\mathcal{M}_{\mathrm{E,t}} \leftarrow 1$. We select $\mathcal{T}_{1,\mathrm{t}} \leftarrow [800, 1400]$ms and $\mathcal{T}_{2,\mathrm{t}} \leftarrow [50, 120]$ms to correspond with WM and GM regions of interest (ROIs) at 3T [64, 65].We take $\mathcal{K}_{\mathrm{t}} \leftarrow [0.9, 1.1]$ to account for 10% spatial variation in flip angle. Broadened ranges $\mathcal{X}_{\mathrm{b}} \leftarrow 1\times[400, 2000]\mathrm{ms}\times[40, 200]$ms and $\mathcal{K}_{\mathrm{b}} \leftarrow [0.5, 2]$ are constructed to encourage solutions robust to a wide range of object parameters. We assume constant noise variance $\sigma_1^2 = \cdots = \sigma_D^2 := \sigma^2$, where $\sigma^2 \leftarrow 1.49 \times 10^{-7}$ is selected to reflect measurements from normalized phantom datasets (*cf.* Sections IV.B.1 and S.V.A-S. V.B for acquisition details). Lastly, we set $\delta \leftarrow 0.01$ to select a robust scan parameter $\mathbf{P}^*$ with associated worst-case cost $\tilde{\Psi}^{\mathrm{t}}(\mathbf{P}^*)$ within 1% of global optimum $\tilde{\Psi}^{\mathrm{t}}(\check{\mathbf{P}})$.

### C. Scan Profile Comparisons

We solve (6) and (9) via grid search to allow illustration (§S.I in Supplement[4]) of $\tilde{\Psi}^{\mathrm{t}}(\mathbf{P})$ as well as worst-case $T_1$, $T_2$ standard deviations $\tilde{\sigma}^{\mathrm{t}}_{T_1}(\mathbf{P})$ and $\tilde{\sigma}^{\mathrm{t}}_{T_2}(\mathbf{P})$, each defined as

[4]Supplementary material is available in the /media tab on IEEEXplore.

$$\tilde{\sigma}^{\mathrm{t}}_{T_1}(\mathbf{P}) := \max_{\substack{\mathbf{x}\in\mathscr{X}_{\mathrm{b}} \\ \boldsymbol{\nu}\in\mathscr{N}_{\mathrm{b}}}} \sigma_{T_1}(\mathbf{x};\boldsymbol{\nu},\mathbf{P}) \quad \text{and} \tag{21}$$

$$\tilde{\sigma}^{\mathrm{t}}_{T_2}(\mathbf{P}) := \max_{\substack{\mathbf{x}\in\mathscr{X}_{\mathrm{b}} \\ \boldsymbol{\nu}\in\mathscr{N}_{\mathrm{b}}}} \sigma_{T_2}(\mathbf{x};\boldsymbol{\nu},\mathbf{P}), \tag{22}$$

where $\boldsymbol{\sigma}_{T_1}(\mathbf{x};\ \boldsymbol{\nu},\mathbf{P})$ and $\boldsymbol{\sigma}_{T_2}(\mathbf{x};\ \boldsymbol{\nu},\mathbf{P})$ are corresponding diagonal elements of inverse Fisher matrix $\mathbf{I}^{-1}(\mathbf{x};\ \boldsymbol{\nu},\mathbf{P})$. Grid searches for the (2, 1), (1, 1), and (0, 2) profiles each took about 4, 43, and 28 minutes, respectively. All experiments described hereafter were carried out using MATLAB® R2013a on a 3.5GHz desktop with 32GB RAM.

Table I compares optimized scan parameters for profiles consisting of (2, 1), (1, 1), and (0, 2) SPGR and DESS scans, respectively. In addition to $\tilde{\sigma}^{\mathrm{t}}_{T_1}(\mathbf{P}^*)$ and $\tilde{\sigma}^{\mathrm{t}}_{T_2}(\mathbf{P}^*)$, Table I presents analogous worst-case standard deviations $\tilde{\sigma}^{\mathrm{b}}_{T_1}(\mathbf{P})$ and $\tilde{\sigma}^{\mathrm{b}}_{T_2}(\mathbf{P})$ over $\mathscr{X}_{\mathrm{b}} \times \mathscr{K}_{\mathrm{b}}$ to show how each estimator degrades over the broadened object parameter range. When viewed over tight range $\mathscr{X}_{\mathrm{t}} \times \mathscr{K}_{\mathrm{t}}$, the (0, 2) profile provides a 11.5% reduction in worst-case cost over the other choices. Extending to broadened range $\mathscr{X}_{\mathrm{b}} \times \mathscr{K}_{\mathrm{b}}$, this reduction grows dramatically to 31.4%. We thus observe that while the different optimized profiles afford similar estimator precision over a narrow range of interest, the (0, 2) profile may be preferable due to its robustness to a wide range of object parameters.

As the DESS sequence has already found success for $T_2$ mapping from even one scan [35], it is reassuring but unsurprising that our analysis finds two DESS scans to yield the most precise $T_2$ estimates. More interestingly, our methods suggest that, with a minimum $C_{\mathrm{DESS}} = 2$ scans, DESS can be used to simultaneously estimate $T_1$ as well. In fact, for certain choices of parameter ranges, a second DESS scan is predicted to afford $\hat{T}_1$ precision comparable to two SPGR scans.

## IV. Experimental Validation and Results

To test our approach to optimized scan design (described in Section II.B), we next estimate $\mathbf{T}_1$ and $\mathbf{T}_2$ maps (using maximum-likelihood (ML) and regularized least squares (RLS) methods detailed in Section S.II) from datasets collected using the scan profiles optimized in Section III. In Section IV.A, we study estimator statistics from simulated data. In Sections IV.B–IV.C, we progress to phantom and *in vivo* datasets to evaluate scan profile performance and estimator robustness under increasingly complex settings. For the latter experiments, we use reference parameter maps from classical (long) pulse sequences, in lieu of ground truth maps.

### A. Numerical Simulations

We select $T_1$ and $T_2$ WM and GM values based on previously reported measurements at 3T [64, 65] and extrapolate other unimportant latent object parameters $M_0$ and $T_2^*$ from measurements at 1.5T [66]. We assign these parameter values to the discrete anatomy of the BrainWeb digital phantom [66, 67] to create ground truth $\mathbf{M}_0$, $\mathbf{T}_1$, $\mathbf{T}_2$, and $\mathbf{T}_2^*$ maps. We then choose acquisition parameters based on Table I (with fixed $T_E$ = 4.67ms) and apply models (20) and (15)–(16) to the 81st slices of these true maps to compute noiseless 217×181 SPGR and DESS image-domain data, respectively.

For each scan profile, we corrupt the corresponding (complex) noiseless dataset $\mathbf{F}$ with additive complex Gaussian noise, whose variance $\sigma^2 \leftarrow 1.49 \times 10^{-7}$ is set to match CRB calculations. This yields realistically noisy datasets $\mathbf{Y}$ ranging from 105–122 SNR, where SNR is defined here as

$$\mathrm{SNR}(\mathbf{F}, \boldsymbol{Y}) := \frac{\|\mathbf{F}\|_F}{\|\boldsymbol{Y} - \mathbf{F}\|_F}. \quad (23)$$

We use each profile's noisy magnitude dataset $|\mathbf{Y}|$ to compute estimates $\hat{\mathbf{M}}_E$, $\hat{\mathbf{T}}_1$, and $\hat{\mathbf{T}}_2$ (images and histograms in Section S.III). We then evaluate estimator bias and variance from latent ground truth $\mathbf{T}_1$ and $\mathbf{T}_2$ maps.

In these simulations, we intentionally neglect to model a number of physically realistic effects because their inclusion would complicate study of estimator statistics. First and foremost, we assume knowledge of a uniform transmit field, to avoid confounding $B_1^+$ and $T_1$, $T_2$ estimation errors. For a similar reason, spatial variation in the sensitivity of a single receive coil is also not considered. We omit modeling partial volume effects to ensure deterministic knowledge of WM and GM ROIs. We will explore the influence of these (and other) nuisance effects on scan design in later subsections.

To isolate bias due to estimator nonlinearity from regularization bias, we minimize the ML initialization cost (S.1) only, and do not proceed to solve RLS problem (S.2). This permits consideration of $T_1$, $T_2$ estimation from each of the 7733 WM or 9384 GM data points as voxel-wise independent realizations of the same estimation problem. To minimize quantization bias, we optimize (S.1) using a very finely spaced dictionary of signal vectors from 1000 $T_1$ and $T_2$ values logarithmically spaced between $[10^2, 10^{3.5}]$ and $[10^1, 10^{2.5}]$, respectively. Using $10^6$ dictionary elements, solving (S.1) took less than 7 minutes for each tested scan design $\mathbf{P}^*$.

Table II[5] verifies that, despite model nonlinearity and Rician noise, estimation bias in WM- and GM-like voxels is negligible. Sample standard deviations are consistent with $\tilde{\sigma}^{\mathrm{t}}_{T_1}$ and $\tilde{\sigma}^{\mathrm{t}}_{T_2}$

[5]Each sample statistic presented hereafter is rounded off to the highest place value of its corresponding uncertainty measure. For simplicity, each uncertainty measure is itself endowed one extra significant figure. Decimal points indicate the significance of trailing zeros.

(*cf.* Table I). In WM and GM, we observe that the (1, 1) and (0, 2) profiles afford high $\hat{\mathbf{T}}_1^{\mathrm{ML}}$ precision, while the (2, 1) and (0, 2) scans afford high $\hat{\mathbf{T}}_2^{\mathrm{ML}}$ precision. In agreement with the predictions of $\tilde{\Psi}^{\mathrm{t}}$ and $\tilde{\Psi}^{\mathrm{b}}$, these simulation studies suggest that at these SNR levels, an optimized profile containing 2 DESS scans can permit $\mathbf{T}_1$ and $\mathbf{T}_2$ estimation precision in WM and GM comparable to optimized profiles containing SPGR/DESS combinations.

## B. Phantom Experiments

This subsection describes two experiments. In the first experiment, we compare the SPGR/DESS scan profiles described in Table I (as well as a reference profile consisting of IR and SE scans) against nuclear magnetic resonance (NMR) measurements from the National Institute for Standards and Technology (NIST) [68]. These measurements provide information about *ROI sample means* and *ROI sample standard deviations* (Fig. 1), which we define as first- and second-order statistics computed across voxels within an ROI. In the second experiment, we repeat the SPGR/DESS scan profiles 10 times and compute *sample standard deviation maps* across repetitions (not shown). Taking ROI sample means of these maps gives *pooled sample standard deviations* (Table III), which indicate relative scan profile precision.

**1) Within-ROI Statistics—**We acquire combinations of (2, 1), (1, 1), and (0, 2) SPGR and DESS coronal scans of a High Precision Devices® MR system phantom $T_2$ array. For each scan profile, we prescribe the optimized flip angles $\hat{\boldsymbol{\alpha}}_0$ and repetition times $\hat{\mathbf{T}}_{\mathrm{R}}$ listed in Table I, and hold all other scan parameters fixed. We achieve the desired nominal flip angles by scaling a 20mm slab-selective Shinnar-Le Roux excitation [69], of duration 1.28ms and time-bandwidth product 4. For each DESS (SPGR) scan, we apply 2 (10) spoiling phase cycles over a 5mm slice thickness. We acquire all steady-state phantom and *in vivo* datasets with a 256 × 256 × 8 matrix over a 240 × 240 × 30 $\mathrm{mm}^3$ field of view (FOV). Using a 31.25kHz readout bandwidth, we acquire all data at minimum $T_{\mathrm{E}} \leftarrow$ 4.67ms before or after RF excitations. To avoid slice-profile effects, we sample **k**-space over a 3D Cartesian grid. After Fourier transform of the raw datasets, only one of the excited image slices is used for subsequent parameter mapping. Including time to reach steady-state, each steady-state scan profile requires 1m37s scan time.

To validate a reference scan profile for use in *in vivo* experiments, we also collect 4 IR and 4 SE scans. For (phase-sensitive, SE) IR, we hold ($T_{\mathrm{R}}$, $T_{\mathrm{E}}$) $\leftarrow$ (1400, 14)ms fixed and vary (adiabatic) inversion time $T_{\mathrm{I}} \in$ {50, 150, 450, 1350}ms across scans. For SE, we similarly hold $T_{\mathrm{R}} \leftarrow$ 1000ms fixed and vary echo time $T_{\mathrm{E}} \in$ {10, 30, 60, 150}ms across scans. We prescribe these scan parameters to acquire 256×256 datasets over the same 240 × 240 × 5 $\mathrm{mm}^3$ slice processed from the SPGR/DESS datasets. Each IR and SE scan requires 5m58s and 4m16s, for a total 40m58s scan time.

We additionally collect a pair of Bloch-Siegert shifted 3D SPGR scans for separate $\mathbf{B}_1^+$ estimation [70]. We insert a 9ms Fermi pulse (peak amplitude $B_1^{\mathrm{pk}} \leftarrow 0.075\mathrm{G}$) at ±8 kHz off-resonance into an SPGR sequence immediately following on-resonant excitation. We estimate regularized $\hat{\mathbf{B}}_1^+$ maps [71] from the resulting pair of datasets. We then estimate flip

angle variation $\hat{\boldsymbol{\kappa}}$ as $\hat{\mathbf{B}}_1^+ / B_1^{\mathrm{pk}}$, calibrate $\hat{\boldsymbol{\kappa}}$ (via separate measurements described in Section S.IV), and thereafter take $\boldsymbol{\kappa}$ as known. For consistency, we account for flip angle variation when estimating $\mathbf{T}_1$ and $\mathbf{T}_2$ from both the candidate (SPGR/DESS) and reference (IR/SE) aforementioned scan profiles. With a repetition time of 21.7ms, this $\mathbf{B}_1^+$ mapping acquisition requires 1m40s total scan time.

Fig. 1 plots sample means and sample standard deviations computed within circular ROIs of phantom $\mathbf{T}_1$ and $\mathbf{T}_2$ ML estimates (reconstruction details, analogous plots for RLS estimates, and images in Sections S.V.A–S.V.C). The highlighted orange and yellow parameter spaces correspond to design ranges $\mathscr{X}_{\mathrm{t}}$ and $\mathscr{X}_{\mathrm{b}}$. $\mathbf{T}_1$ estimates from both the candidate (2, 1), (1, 1), and (0, 2) (SPGR, DESS) and reference (4, 4) (IR, SE) profiles are in reasonable agreement with NIST estimates [68] across the vial range. $\mathbf{T}_2$ estimates from all profiles are also in good agreement with NIST for vials within $\mathscr{X}_{\mathrm{b}}$. SPGR/DESS profiles likely underestimate large $T_2$ values (≥200ms) due to greater influence of diffusion in DESS [59–61]. SPGR/DESS profiles possibly overestimate and the IR/SE profile likely underestimates short (≤30ms) and very short (≤15ms) $T_2$ values, respectively, due to poorly conditioned estimation.

**2) Across-Repetition Statistics—**In a second study, we repeat the (2, 1), (1, 1), and (0, 2) scan profiles 10 times each and separately estimate $\mathbf{T}_1$ and $\mathbf{T}_2$ for each repetition of each scan profile. We then estimate the standard deviation across repetitions on a per-voxel basis, to produce sample standard deviation maps for each profile. Each ROI voxel of the sample standard deviation map is a better estimate of the *population standard deviation* (which the CRB characterizes) than the ROI sample standard deviation from a single repetition, because the latter estimate is contaminated with slight spatial variation of voxel population means (due to imaging non-idealities such as Gibbs ringing due to **k**-space truncation).

Table III reports pooled sample standard deviations and pooled standard errors of the sample standard deviations (computed via expressions in [72]) for phantom vials within (or nearly within) tight design range $\mathscr{X}_{\mathrm{t}}$ (marked orange in Fig. S.7). Due to error propagation from coil combination and $\hat{\boldsymbol{\kappa}}$ estimation, pooled ML sample standard deviations cannot be compared *in magnitude* to worst-case predicted standard deviations (Table I); however, *trends* of empirical and theoretical standard deviations are overall similar. In particular, the optimized (0, 2) DESS-only scan profile affords $T_1$ ML estimation precision (in vials whose $T_1$, $T_2$ is similar to that of WM/GM) comparable to optimized (2, 1) and (1, 1) mixed (SPGR, DESS) profiles. Also in agreement with predictions, the optimized (2, 1) and (0, 2) profiles afford greater $T_2$ ML estimation precision than the optimized (1, 1) profile.

## C. In Vivo Experiments

In a single long study of a healthy volunteer, we acquire the same optimized scan profiles containing (2, 1), (1, 1), and (0, 2) SPGR and DESS scans (*cf.* Table I), as well as the reference profile containing (4, 4) IR and SE scans. We obtain axial slices from a 32-channel Nova Medical® receive head array. To address bulk motion between acquisitions and to compare within-ROI statistics, we rigidly register each coil-combined image to an IR image (details in Section S.V.D) prior to parameter mapping. All acquisition (*cf.* Section IV.B.1)

and reconstruction (*cf.* Sections S.V.A–S.V.B) details are otherwise the same as in phantom experiments.

Fig. 2 compares brain $\mathbf{T}_1$ and $\mathbf{T}_2$ ML estimates from optimized scan profiles (Fig. S.9 and Fig. S.10 provide corresponding colorized and grayscale RLS estimates, respectively). Though in-plane motion is largely compensated via registration, through-plane motion and non-bulk motion likely persist, and will influence ROI statistics. Due to motion (and scan duration) considerations, we examine within-ROI statistics from a single repetition as in Section IV.B.1, and do not attempt across-repetition statistics as in Section IV.B.2.

Visually, $\hat{\mathbf{T}}_1$ maps from steady-state profiles exhibit similar levels of contrast in WM/GM regions well away from cerebrospinal fluid (CSF) as that seen in the reference $\hat{\mathbf{T}}_1$ estimate. Since we did not optimize any scan profiles for estimation in high-$T_1$ regions, it is expected that greater differences may emerge in voxels containing or nearby CSF. In particular, $\mathbf{T}_1$ is significantly underestimated within and near CSF by the (0, 2) DESS-only profile. This suggests that with the signal models used in this work, including at least one SPGR scan in an optimized profile may offer greater protection against estimation bias in high-$T_1$ regions.

Table IV summarizes within-ROI sample means and sample standard deviations computed[6] over four separate WM ROIs containing 96, 69, 224, and 148 voxels and one pooled cortical GM ROI containing 156 voxels (*cf.* Fig. 2). Within-ROI $\hat{\mathbf{T}}_1$ sample standard deviations are comparable across steady-state profiles. In agreement with Table I, $\mathbf{T}_2$ estimates from the optimized (1, 1) scan profile exhibit higher within-ROI sample variation than corresponding (2, 1) and (0, 2) $\hat{\mathbf{T}}_2$ maps.

In most cases, $\hat{\mathbf{T}}_1$ within-ROI sample means from optimized SPGR/DESS scan profiles do not deviate substantially from each other or from reference IR/SE measurements. Two notable exceptions are $\hat{T}_1^{\mathrm{ML}}$ in anterior left and posterior right WM from (1, 1) and (0, 2) profiles: these estimates are significantly lower and higher than analogous estimates from other profiles, respectively. Results thus suggest that the optimized (2, 1) scan profile yields WM $\hat{T}_1^{\mathrm{ML}}$ estimates that are more consistently similar to IR WM $\hat{T}_1^{\mathrm{ML}}$ estimates than other optimized SPGR/DESS profiles.

Systematic differences in $\hat{\mathbf{T}}_2$ sample means are evident across scan profiles, particularly within WM ROIs. Curiously, the (1, 1) profile agrees most consistently (in WM/GM $\hat{T}_2^{\mathrm{ML}}$ within-ROI sample mean) with reference estimates, though with relatively high sample variation. The (2, 1) and (0, 2) SPGR/DESS profiles produce consistently lower WM $\hat{T}_2^{\mathrm{ML}}$ than the reference IR/SE profile, though the (0, 2) profile is in reasonable agreement with other steady-state estimates [73].

These discrepancies may due to differences in sensitivity to multi-compartmental relaxation [74]. Specifically, different signal models with different scan parameter choices might be

[6]We have taken effort to try and select ROIs that reflect expected anatomy in all coil-combined and registered images, including adjacent slices in images from 3D acquisitions. However, we acknowledge the possibility of some contamination across tissue boundaries, especially WM and/or CSF contamination into cortical GM.

more or less sensitive to the model mismatch incurred by neglecting to distinguish the multiple $T_2$ components within each voxel. Section S.VI studies $\mathbf{T}_2$ estimation bias due to multi-compartmental relaxation in more detail.

## V. Discussion and Future Work

Phantom experiments show that optimized scan profiles consisting of (2, 1), (1, 1), and (0, 2) (SPGR, DESS) scans yield accurate WM/GM $T_1$, $T_2$ estimates, and that empirical precision trends across profiles agree reasonably with CRB-based predictions. However, *in vivo* experiments reveal that even with scan optimization, it may be challenging to achieve clinically viable levels of precision from the aforementioned steady-state profiles, at least at 3T. At the expense of greater scan time, it is of course possible that optimized profiles containing greater numbers of SPGR, DESS, and/or other steady-state scans can provide clinically acceptable precision levels. For these and other more complicated scan profiles, estimator dependence on scan parameters becomes even less intuitive, increasing the need for scan design.

The proposed scan design framework addresses spatial variation in object parameters through a min-max design criterion. The min-max criterion guarantees an upper bound on a weighted sum of variances and assumes no prior knowledge of distributions. However, in general it is non-differentiable in $\mathbf{P}$, precluding gradient-based optimization. Furthermore, it is conservative by nature, and often selects scan parameters based on corner cases of the object parameter space. To reduce the influence of corner cases, it may be desirable to instead construct a cost function related to the coefficient of variation as in [44, 46–48], perhaps by setting parameter weights $\mathbf{W}^{-1} \leftarrow \text{diag}(\mathbf{x})$ for $\mathbf{x} \neq 0$ in (5).

As a less conservative alternative to min-max design, other recent works [50, 51] have addressed object parameter spatial variation by instead constructing cost functions related to the Bayesian CRB [75], which characterizes the expected precision with respect to a prior distribution on object parameters. Bayesian cost functions are usually differentiable and can also, with appropriate priors, penalize object parameter coefficients of variation instead of variances, as in [50]. However, prior distributions are generally unknown, and may need to be estimated from data, as in [51].

Careful calibration of flip angle scaling $\boldsymbol{\kappa}$ is essential for accurate $\mathbf{T}_1$,$\mathbf{T}_2$ estimation from SPGR/DESS scan profiles. In this work, we estimate $\boldsymbol{\kappa}$ from *separate* acquisitions and adjust nominal flip angles prior to reconstruction, but acknowledge that non-idealities in those separate acquisitions may themselves cause resultant $\hat{\mathbf{B}}_1^+$ errors to propagate into our $\mathbf{T}_1$,$\mathbf{T}_2$ estimates. To reduce error propagation, it may be desirable to instead design scan profiles to permit *joint* estimation of $\boldsymbol{\kappa}$, in addition to other latent object parameters. Unfortunately, we find that optimizing the (2, 1) or (0, 2) profile to allow for four-parameter $\mathbf{x}(\mathbf{r}) := [M_E(\mathbf{r}), T_1(\mathbf{r}), T_2(\mathbf{r}), \kappa(\mathbf{r})]^\top$ estimation results in unacceptably high amplification of the worst-case $T_1$ standard deviation. (Incidentally, precise $\mathbf{T}_2$ ML and RLS estimation alone from the (2, 1) or (0, 2) profile is possible [42].) It remains an open scan design question as to whether time spent collecting Bloch-Siegert data for separate $\mathbf{B}_1^+$ mapping could instead be better spent collecting additional SPGR, DESS, and/or other data for joint estimation.

By working with closed-form signal expressions, we neglect to model several higher-order effects. However, it is apparent that the nonlinear estimation procedures required for many mapping problems can amplify the influence of these secondary effects, often inducing substantial bias. Since the CRB (as described) applies only to unbiased estimators, it is thus desirable to use signal models that are as complete as possible for CRB-based scan design. In theory, scan optimization approach (9) is even compatible with acquisitions where a closed-form model relating data to latent and scan parameters is unknown, as in [22, 76]. In practice, difficulties arise in efficient computation of signal gradients required in (3), which may demand more specialized techniques, as in [77]. Designing scan profiles involving such complex signal models would likely necessitate optimization techniques more involved than the simple grid searches used in this work.

## VI. Conclusion

We have introduced a CRB-inspired min-max optimization approach to aid robust, application-specific MR scan selection and optimization for precise parameter estimation. As a detailed example, we have optimized combinations of fast SPGR and DESS scans for $T_1$, $T_2$ relaxometry in WM and GM regions of the human brain at 3T. Numerical simulations show that at typical noise levels and with accurate flip angle prior knowledge, WM- and GM-like $T_1$, $T_2$ ML estimates from optimized scans are nearly unbiased, and so worst-case CRB predictions yield reliable bounds on ROI sample variances. Phantom accuracy experiments show that optimized combinations of (2, 1), (1, 1), or (0, 2) (SPGR, DESS) scans are in excellent agreement with NIST and IR/SE measurements over the designed latent object parameter range of interest. Phantom precision experiments show that these SPGR/DESS combinations exhibit trends in pooled sample standard deviations that reasonably reflect CRB predictions. *In vivo* experiments suggest that with optimization, the (0, 2) profile can yield comparable $\hat{\mathbf{T}}_1$, $\hat{\mathbf{T}}_2$ precision to the more conventional (2, 1) [42] scan profile in well-isolated WM/GM ROIs; however, the (0, 2) $\mathbf{T}_1$ estimates are unreliable within and near the CSF and do not agree with IR measurements in WM as consistently as the (2, 1) profile. This and other disagreements across profiles *in vivo* may be attributable to differences in signal model sensitivities to neglected higher-order effects. Nevertheless, this simple example application illustrates that scan optimization may enable new parameter mapping techniques from established pulse sequences.

## Supplementary Material

Refer to Web version on PubMed Central for supplementary material.

## Acknowledgments

This work was supported in part by the National Institutes of Health (NIH) under Grant P01 CA87634, and in part by the University of Michigan's MCubed funding program.

The authors thank Dr. Kathryn Keenan and Dr. Stephen Russek at NIST for generously lending a prototype [78] (used in initial experiments) of the High Precision Devices® MR system phantom, and for sharing an early preprint of [68]. The authors also thank the reviewers for their helpful suggestions.

## References


1. Cheng HLM, Stikov N, Ghugre NR, Wright GA. Practical medical applications of quantitative MR relaxometry. J Mag Res Im. Oct; 2012 36(4):805–24.
2. Larsson HBW, Frederiksen J, Kjaer L, Henriksen O, Olesen J. In vivo determination of T1 and T2 in the brain of patients with severe but stable multiple sclerosis. Mag Res Med. May; 1988 7(1):43–55.
3. Kurki T, Lundbom N, Komu M, Kormano M. Tissue characterization of inter cranial tumors by magnetization transfer and spin-lattice relaxation parameters in vivo. J Mag Res Im. Aug; 1996 6(4):573–9.
4. Englund E, Brun A, Gyorffy-Wagner Z, Larsson E, Persson B. Relaxation times in relation to grade of malignancy and tissue necrosis in astrocytic gliomas. Mag Res Im. 1986; 4(5):425–9.
5. Siemonsen S, Mouridsen K, Holst B, Ries T, Finsterbusch J, Thomalia G, Ostergaard L, Fiehler J. Quantitative T2 values predict time from symptom onset in acute stroke patients. Stroke. May; 2009 40(5):1612–6. [PubMed: 19325153]
6. DeWitt LD, Kistler JP, Miller DC, Richardson EP, Buonanno FS. NMR-neuropathologic correlation in stroke. Stroke. 1987; 18(2):342–51. [PubMed: 3564090]
7. Matzat SJ, Tiel JV, Gold GE, Oei EHG. Quantitative MRI techniques of cartilage composition. Quant Imaging Med Surg. Jun; 2013 3(3):162–74. [PubMed: 23833729]
8. Mosher TJ, Dardzinski BJ. Cartilage MRI T2 relaxation time mapping: overview and applications. Semin Musculoskelet Radiol. 2004; 8(4):355–68. [PubMed: 15643574]
9. Guo H, Au W-Y, Cheung JS, Kim D, Jensen JH, Khong P-L, Chan Q, Chan KC, Tosti C, Tang H, Brown TR, Lam WWM, Ha S-Y, Brittenham GM, Wu EX. Myocardial T2 quantification in patients with iron overload at 3 Tesla. J Mag Res Im. Aug; 2009 30(2):394–400.
10. Giri S, Chung YC, Merchant A, Mihai G, Rajagopalan S, Raman SV, Simonetti OP. T2 quantification for improved detection of myocardial edema. Cardiovasc Magn Reson. 2009; 11(1): 56–68.
11. Look DC, Locker DR. Time saving in measurement of NMR and EPR relaxation times. Rev Sci Instrum. Feb; 1970 41(2):250–1.
12. Carr HY, Purcell EM. Effects of diffusion on free precession in nuclear magnetic resonance experiments. Phys Rev. May; 1954 94(3):630–8.
13. Stehling MK, Turner R, Mansfield P. Echo-planar imaging: magnetic resonance imaging in a fraction of a second. Science. Oct; 1991 254(5028):43–50. [PubMed: 1925560]
14. Ahn CB, Kim JH, Cho ZH. High-speed spiral-scan scho planar NMR imaging - I. IEEE Trans Med Imag. Mar; 1986 5(1):2–7.
15. Meyer CH, Hu BS, Nishimura DG, Macovski A. Fast spiral coronary artery imaging. Mag Res Med. Dec; 1992 28(2):202–13.
16. Kay I, Henkelman RM. Practical Implementation and Optimization of One-shot T1 imaging. Mag Res Med. Dec; 1991 22(2):414–24.
17. Gowland PA, Leach MO. Fast and accurate measurements of T1 using a multi-readout single inversion-recovery sequence. Mag Res Med. Jul; 1992 26(1):79–88.
18. Messroghli DR, Radjenovic A, Kozerke S, Higgins DM, Sivananthan MU, Ridgway JP. Modified Look-Locker inversion recovery (MOLLI) for high-resolution $T_1$ mapping of the heart. Mag Res Med. Jul; 2004 52(1):141–6.
19. Stehling MK, Ordidge RJ, Coxon R, Mansfield P. Inversion-recovery Echo-planar imaging (IR-EPI) at 0.5T. Mag Res Med. Mar; 1990 13(3):514–7.
20. Bonny JM, Zanca M, Boire JY, Veyre A. T2 maximum likelihood estimation from multiple spin-echo magnitude images. Mag Res Med. Aug; 1996 36(2):287–93.
21. Kumar D, Nguyen TD, Gauthier SA, Raj A. Bayesian algorithm using spatial priors for multiexponential T2 relaxometry from multiecho spin echo MRI. Mag Res Med. Nov; 2012 68(5): 1536–43.
22. Ben-Eliezer N, Sodickson DK, Block KT. Rapid and accurate T2 mapping from multi–spin-echo data using Bloch-simulation-based reconstruction. Mag Res Med. Feb; 2015 73(2):809–17.

23. Nguyen TD, Wisnieff C, Cooper MA, Kumar D, Raj A, Spincemaille P, Wang Y, Vartanian T, Gauthier SA. T2prep three-dimensional spiral imaging with efficient whole brain coverage for myelin water quantification at 1.5 tesla. Mag Res Med. Mar; 2012 67(3):614–21.
24. Majumdar S, Orphanoudakis SC, Gmitro A, O'Donnell M, Gore JC. Error in the measurements of T2 using multiple-echo MRI techniques: 1. Effect of radiofrequency pulse imperfections. Mag Res Med. Jun; 1986 3(3):397–417.
25. Majumdar S, Orphanoudakis SC, Gmitro A, O'Donnell M, Gore JC. Error in the measurements of T2 using multiple-echo MRI techniques: 2. Effects of static field inhomogeneity. Mag Res Med. Aug; 1986 3(4):562–74.
26. Farzaneh F, Riederer SJ, Pelc NJ. Analysis of T2 limitations and off-resonance effects on spatial resolution and artifacts in echo-planar imaging. Mag Res Med. Apr; 1990 14(1):123–39.
27. Hinshaw WS. Image formation by nuclear magnetic resonance: The sensitive point method. J Appl Phys. Aug.1976 47(8):3709.
28. Scheffler K. A pictorial description of steady-states in rapid magnetic resonance imaging. Concepts in Magnetic Resonance. 1999; 11(5):291–304.
29. Deoni SCL, Rutt BK, Peters TM. Rapid combined T1 and T2 mapping using gradient recalled acquisition in the steady state. Mag Res Med. Mar; 2003 49(3):515–26.
30. Chang LC, Koay CG, Basser PJ, Pierpaoli C. Linear least-squares method for unbiased estimation of T1 from SPGR signals. Mag Res Med. Aug; 2008 60(2):496–501.
31. Fram EK, Herfkens RJ, Johnson GA, Glover GH, Kaaris JP, Shimakawa A, Perkins TG, Pelc NJ. Rapid calculation of T1 using variable flip angle gradient refocused imaging. Mag Res Im. 1987; 5(3):201–8.
32. Wang H, Cao Y. Spatially regularized T1 estimation from variable flip angles MRI. Med Phys. Jul; 2012 39(7):4139–48.
33. Deoni SCL, Ward HA, Peters TM, Rutt BK. Rapid $T_2$ estimation with phase-cycled variable nutation steady-state free precession. Mag Res Med. Aug; 2004 52(2):435–9.
34. Deoni SCL. Transverse relaxation time (T2) mapping in the brain with off-resonance correction using phase-cycled steady-state free precession imaging. J Mag Res Im. Aug; 2009 30(2):411–7.
35. Welsch GH, Scheffler K, Mamisch TC, Hughes T, Millington S, Deimling M, Trattnig S. Rapid estimation of cartilage T2 based on double echo at steady state (DESS) with 3 Tesla. Mag Res Med. Aug; 2009 62(2):544–9.
36. Heule R, Ganter C, Bieri O. Rapid estimation of cartilage T2 with reduced T1 sensitivity using double echo steady state imaging. Mag Res Med. Mar; 2014 71(3):1137–43.
37. Stöcker T, Keil F, Vahedipour K, Brenner D, Pracht E, Shah NJ. MR parameter quantification with magnetization-prepared double echo steady-state (MP-DESS). Mag Res Med. Jul; 2014 72(1): 103–11.
38. Heule R, Ganter C, Bieri O. Triple echo steady-state (TESS) relaxometry. Mag Res Med. Jan; 2014 71(1):230–7.
39. Bruder H, Fischer H, Graumann R, Deimling M. A new steady-state imaging sequence for simultaneous acquisition of two MR images with clearly different contrasts. Mag Res Med. May; 1988 7(1):35–42.
40. Gyngell ML. The steady-state signals in short-repetition-time sequences. J Mag Res. Feb; 1989 81(3):474–83.
41. Hänicke W, Vogel HU. An analytical solution for the SSFP signal in MRI. Mag Res Med. Apr; 2003 49(4):771–5.
42. Nataraj G, Nielsen J-F, Fessler JA. Model-based estimation of T2 maps with dual-echo steady-state MR imaging. Proc IEEE Intl Conf on Image Processing. 2014:1877–81.
43. Weiss GH, Gupta RK, Ferretti JA, Becker ED. The choice of optimal parameters for measurement of spin-lattice relaxation times. I. Mathematical formulation. J Mag Res. Feb; 1980 37(3):369–79.
44. Zhang Y, Yeung HN, O'Donnell M, Carson PL. Determination of sample time for T1 measurement. J Mag Res Im. May; 1998 8(3):675–81.
45. Wang HZ, Riederer SJ, Lee JN. Optimizing the precision in T1 relaxation estimation using limited flip angles. Mag Res Med. Nov; 1987 5(5):399–416.

46. Jones JA, Hodgkinson P, Barker AL, Hore PJ. Optimal sampling strategies for the measurement of spin-spin relaxation times. J Mag Res B. Oct; 1996 113(1):25–34.
47. Imran J, Langevin François, Saint-Jalmes Hervé. Two-point method for T1 estimation with optimized gradient-echo sequence. Mag Res Im. Nov; 1999 17(9):1347–56.
48. Deoni SCL, Peters TM, Rutt BK. Determination of optimal angles for variable nutation proton magnetic spin-lattice, $T_1$, and spin-spin, $T_2$, relaxation times measurement. Mag Res Med. Jan; 2004 51(1):194–9.
49. Fleysher L, Fleysher R, Liu S, Zaaraoui W, Gonen O. Optimizing the precision-per-unit-time of quantitative MR metrics: Examples for $T_1$, $T_2$, and DTI. Mag Res Med. Feb; 2007 57(2):380–7.
50. Akçakaya M, Weingärtner S, Roujol Sébastien, Nezafat R. On the selection of sampling points for myocardial T1 mapping. Mag Res Med. May; 2015 73(5):1741–53.
51. Lewis CM, Hurley SA, Meyerand ME, Koay CG. Data-driven optimized flip angle selection for T1 estimation from spoiled gradient echo acquisitions. Mag Res Med. 2016 to appear.
52. Fessler JA, Sutton BP. Nonuniform fast Fourier transforms using min-max interpolation. IEEE Trans Sig Proc. Feb; 2003 51(2):560–74.
53. Muckley MJ, Noll DC, Fessler JA. Fast parallel MR image reconstruction via B1-based, adaptive restart, iterative soft thresholding algorithms (BARISTA). IEEE Trans Med Imag. Feb; 2015 34(2): 578–88.
54. Macovski A. Noise in MRI. Mag Res Med. Sep; 1996 36(3):494–7.
55. Lei T. Statistics of MR signals: revisited. Proc SPIE 6510 Medical Imaging 2007: Phys Med Im. 2007:651052.
56. Fisher RA. Theory of statistical estimation. Proc Cambridge Philo- sophical Society. Jul; 1925 22(5):700–25.
57. Cramér, H. Mathematical methods of statistics. Princeton: Princeton Univ. Press; 1946.
58. Chernoff H. Locally optimal designs for estimating parameters. Ann Math Stat. Dec; 1953 24(4): 586–602. [Online]. Available: http://www.jstor.org/stable/2236782.
59. Carney CE, Wong STS, Patz S. Analytical solution and verification of diffusion effect in SSFP. Mag Res Med. Jun; 1991 19(2):240–6.
60. Wu EX, Buxton RB. Effect of diffusion on the steady-state magnetization with pulsed field gradients. J Mag Res. Nov; 1990 90(2):243–53.
61. Kaiser R, Bartholdi E, Ernst RR. Diffusion and field-gradient effects in NMR Fourier spectroscopy. J Chem Phys. Apr; 1974 60(8):2966–79.
62. Bieri O, Scheffler K. SSFP signal with finite RF pulses. Mag Res Med. Nov; 2009 62(5):1232–41.
63. Zur Y, Wood ML, Neuringer LJ. Spoiling of transverse magnetization in steady-state sequences. Mag Res Med. Oct; 1991 21(2):251–63.
64. Wansapura JP, Holland SK, Dunn RS, Ball WS. NMR relaxation times in the human brain at 3.0 Tesla. J Mag Res. Apr; 1999 9(4):531–8.
65. Stanisz GJ, Odrobina EE, Pun J, Escaravage M, Graham SJ, Bronskill MJ, Henkelman RM. $T_1$, $T_2$ relaxation and magnetization transfer in tissue at 3T. Mag Res Med. Sep; 2005 54(3):507–12.
66. Kwan RKS, Evans AC, Pike GB. MRI simulation-based evaluation of image-processing and classification methods. IEEE Trans Med Imag. Nov; 1999 18(11):1085–97.
67. Collins DL, Zijdenbos AP, Kollokian V, Sled JG, Kabani NJ, Holmes CJ, Evans AC. Design and construction of a realistic digital brain phantom. IEEE Trans Med Imag. Jun; 1998 17(3):463–8.
68. Keenan KE, Stupic KF, Boss MA, Russek SE, Chenevert TL, Prasad PV, Reddick WE, Cecil KM, Zheng J, Hu P, Jackson EF. Multi-site, multi-vendor comparison of T1 measurement using ISMRM/NIST system phantom. Proc Intl Soc Mag Res Med. 2016:3290.
69. Pauly J, Le Roux P, Nishimura D, Macovski A. Parameter relations for the Shinnar-Le Roux selective excitation pulse design algorithm. IEEE Trans Med Imag. Mar; 1991 10(1):53–65.
70. Sacolick LI, Wiesinger F, Hancu I, Vogel MW. B1 mapping by Bloch-Siegert shift. Mag Res Med. May; 2010 63(5):1315–22.
71. Sun H, Grissom WA, Fessler JA. Regularized estimation of Bloch-Siegert B1+ Maps in MRI. Proc IEEE Intl Conf on Image Processing. 2014:3646–50.

72. Ahn, S., Fessler, JA. Tech Rep 413. Comm. and Sign. Proc. Lab., Dept. of EECS, Univ. of Michigan; Ann Arbor, MI, 48109-2122: Jul. 2003 Standard errors of mean, variance, and standard deviation estimators. [Online]. Available: http://web.eecs.umich.edu/~fessler/papers/lists/files/tr/stderr.pdf

73. Heule R, Bär P, Mirkes C, Scheffler K, Trattnig S, Bieri O. Triple-echo steady-state T2 relaxometry of the human brain at high to ultra-high fields. NMR in Biomedicine. Sep; 2014 27(9):1037–45. [PubMed: 24986791]

74. Mackay A, Whittall K, Adler J, Li D, Paty D, Graeb D. In vivo visualization of myelin water in brain by magnetic resonance. Mag Res Med. Jun; 1994 31(6):673–7.

75. Gill RD, Levit BY. Applications of the van Trees inequality: A Bayesian Cramér-rao bound. Bernoulli. 1995; 1(1/2):59–79. [Online]. Available: http://www.jstor.org/stable/3318681.

76. Ma D, Gulani V, Seiberlich N, Liu K, Sunshine JL, Duerk JL, Griswold MA. Magnetic resonance fingerprinting. Nature. Mar.2013 495:187–93. [PubMed: 23486058]

77. Zhao B, Haldar J, Setsompop K, Wald LL. Optimal experiment design for magnetic resonance fingerprinting. embc. 2016

78. Russek, SE., Boss, M., Jackson, EF., Jennings, DL., Evelhoch, JL., Gunter, JL., Sorensen, AG. Characterization of NIST/ISMRM MRI system phantom; Proc Intl Soc Mag Res Med. 2012. p. 2456[Online]. Available: http://cds.ismrm.org/protected/12MProceedings/files/2456.pdf

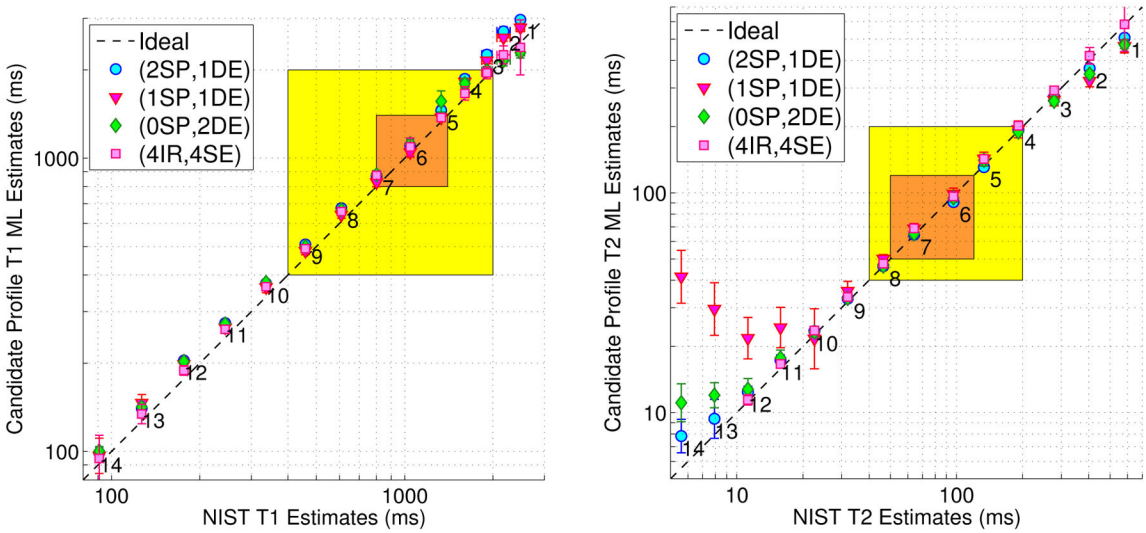


**Fig. 1.**

Phantom within-ROI sample statistics of $\mathbf{T}_1$ and $\mathbf{T}_2$ ML estimates from optimized SPGR/DESS and reference IR/SE scan profiles, vs. NIST NMR measurements [68]. Markers and error bars indicate ROI sample means and ROI sample standard deviations within the 14 labeled and color-coded vials in Fig. S.7. Tight $\mathscr{X}_{\mathrm{t}}$ and broad $\mathscr{X}_{\mathrm{b}}$ latent parameter ranges are highlighted in orange and yellow, respectively. Fig. S.8 provides analogous plots for RLS estimates. Table S.2 replicates sample statistics within Vials 5–8. Our MR measurements are at 293K, while NIST NMR measurements are at 293.00K. Within the designed parameter ranges, estimates from different acquisitions are in reasonable agreement with NIST measurements.

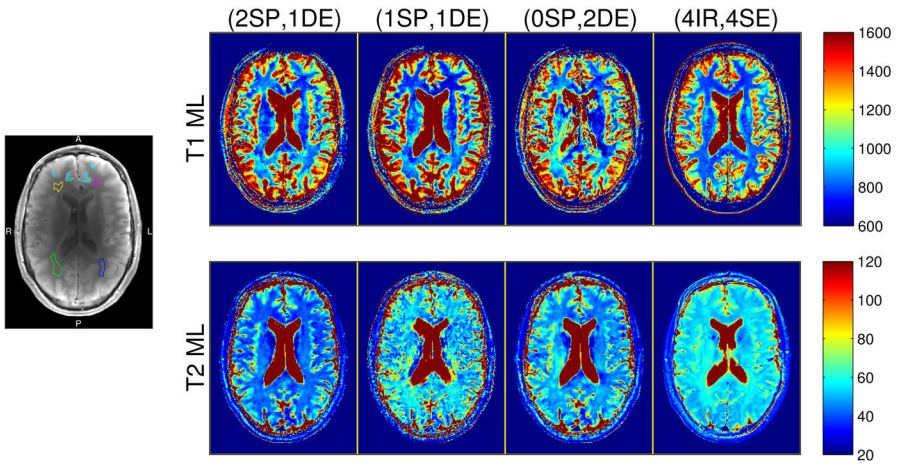


**Fig. 2.**

*Left*: WM and GM ROIs, overlaid on a representative anatomical (coil-combined IR) image. Separate WM ROIs are distinguished with anterior/posterior (A/P) and right/left (R/L) directions. Four small anterior cortical GM polygons are pooled into a single ROI (cyan). *Right*: Colorized $\mathbf{T}_1$ and $\mathbf{T}_2$ ML estimates from the brain of a healthy volunteer. Columns correspond to profiles consisting of (2 SPGR, 1 DESS), (1 SPGR, 1 DESS), (0 SPGR, 2 DESS), and (4 IR, 4 SE) acquisitions. Parameter maps are cropped in post-processing for the purpose of display. Figs. S.9 (colorized) and S.10 (grayscale) provide analogous full-FOV maps estimated via both ML and RLS estimators. Colorbar ranges are in milliseconds.

**TABLE I**

Performance summary of different scan profiles, optimized by solving (9) subject to scan time constraint $T_{R,\max}$ = 41.9ms. The first column defines each profile. The next four columns describe $\mathbf{P}^*$. The latter three pairs of columns show how worst-case $\tilde{\sigma}_{T_1}$ $\tilde{\sigma}_{T_2}$, and $\tilde{\Psi}$ values degrade from tight to broad ranges. Flip angles are in degrees; all other values are in milliseconds.

| **Scan** | $\hat{\alpha}_0^{\mathrm{spgr}}$ | $\hat{\alpha}_0^{\mathrm{dess}}$ | $\hat{T}_R^{\mathrm{spgr}}$ | $\hat{T}_R^{\mathrm{dees}}$ | $\tilde{\sigma}_{T_1}^{\mathrm{t}}(\mathbf{P}^*)$ | $\tilde{\sigma}_{T_1}^{\mathrm{b}}(\mathbf{P}^*)$ | $\tilde{\sigma}_{T_2}^{\mathrm{t}}(\mathbf{P}^*)$ | $\tilde{\sigma}_{T_2}^{\mathrm{b}}(\mathbf{P}^*)$ | $\tilde{\Psi}^{\mathrm{t}}(\mathbf{P}^*)$ | $\tilde{\Psi}^{\mathrm{b}}(\mathbf{P}^*)$ |
|---|---|---|---|---|---|---|---|---|---|---|
| (2, 1) | (15, 5)° | 30° | (12.2, 12.2) | 17.5 | 28 | 154 | **1.3** | 9.1 | 4.0 | 17.7 |
| (1, 1) | 15° | 10° | 13.9 | 28.0 | 27 | 169 | 2.8 | 8.8 | 4.9 | 17.9 |
| (0, 2) | – | (35, 10)° | – | (24.4, 17.5) | **21** | **113** | 1.5 | **6.0** | **3.5** | **12.2** |

**TABLE II**

Sample means ± sample standard deviations of $\mathbf{T}_1$ and $\mathbf{T}_2$ ML estimates in WM and GM ROIs of simulated data, compared across different optimized scan profiles. Sample means exhibit insignificant bias, and sample standard deviations are consistent with worst-case standard deviations $\tilde{\sigma}^{\mathrm{t}}_{T_1}$ and $\tilde{\sigma}^{\mathrm{t}}_{T_2}$ reported in Table I. All values are reported in milliseconds.

| Scan | (2, 1) | (1, 1) | (0, 2) | Truth |
|---|---|---|---|---|
| WM $\hat{T}_1^{\mathrm{ML}}$ | 830 ± 17 | 830 ± 15 | 830 ± 14 | 832 |
| GM $\hat{T}_1^{\mathrm{ML}}$ | 1330 ± 30. | 1330 ± 24 | 1330 ± 24 | 1331 |
| WM $\hat{T}_2^{\mathrm{ML}}$ | 80. ± 1.0 | 80. ± 2.1 | 79.6 ± 0.94 | 79.6 |
| GM $\hat{T}_2^{\mathrm{ML}}$ | 110. ± 1.4 | 110. ± 3.0 | 110. ± 1.6 | 110 |

**TABLE III**

Phantom pooled sample standard deviations ± pooled standard errors of sample standard deviations, from optimized SPGR/DESS scan profiles. Each entry is a measure of uncertainty of a typical voxel's $T_1$ or $T_2$ ML estimate. For sake of brevity, sample statistics corresponding only to phantom vials within (or nearly within) tight design range $\mathscr{T}_t$ (color-coded orange in Fig. S.7) are reported. 'V#' abbreviates vial numbers. All values are reported in milliseconds.

| | (2SP,1DE) | (1SP,1DE) | (0SP,2DE) |
|---|---|---|---|
| V5 $\hat{\sigma}_{\hat{T}_1^{\mathrm{ML}}}(\mathbf{P}^*)$ | 50 ± 12 | 40 ± 10. | 39 ± 9.4 |
| V6 $\hat{\sigma}_{\hat{T}_1^{\mathrm{ML}}}(\mathbf{P}^*)$ | 70 ± 18 | 60 ± 15 | 70 ± 16 |
| V7 $\hat{\sigma}_{\hat{T}_1^{\mathrm{ML}}}(\mathbf{P}^*)$ | 60 ± 13 | 50 ± 13 | 50 ± 13 |
| V8 $\hat{\sigma}_{\hat{T}_1^{\mathrm{ML}}}(\mathbf{P}^*)$ | 23 ± 5.4 | 20. ± 4.7 | 18 ± 4.3 |

| | (2SP,1DE) | (1SP,1DE) | (0SP,2DE) |
|---|---|---|---|
| V5 $\hat{\sigma}_{\hat{T}_2^{\mathrm{ML}}}(\mathbf{P}^*)$ | 2.6 ± 0.63 | 6 ± 1.4 | 3.5 ± 0.84 |
| V6 $\hat{\sigma}_{\hat{T}_2^{\mathrm{ML}}}(\mathbf{P}^*)$ | 1.9 ± 0.46 | 5 ± 1.1 | 2.3 ± 0.54 |
| V7 $\hat{\sigma}_{\hat{T}_2^{\mathrm{ML}}}(\mathbf{P}^*)$ | 1.4 ± 0.34 | 3.4 ± 0.80 | 1.5 ± 0.35 |
| V8 $\hat{\sigma}_{\hat{T}_2^{\mathrm{ML}}}(\mathbf{P}^*)$ | 1.1 ± 0.26 | 3.5 ± 0.84 | 1.4 ± 0.33 |

**TABLE IV**

Within-ROI sample means ± within-ROI sample standard deviations of $\mathbf{T}_1$ and $\mathbf{T}_2$ ML estimates from the brain of a healthy volunteer. Sample statistics are computed within ROIs indicated in Fig. 2. All values are reported in milliseconds.

| | ROI (color) | (2SP,1DE) | (1SP,1DE) | (0SP,2DE) | (4IR,4SE) |
|---|---|---|---|---|---|
| $\hat{T}_1^{\mathrm{ML}}$ | anterior right WM (yellow) | 840 ± 32 | 770 ± 31 | 840 ± 43 | 780 ± 22 |
| | anterior left WM (magenta) | 740 ± 61 | 660 ± 45 | 740 ± 55 | 760 ± 24 |
| | posterior right WM (green) | 890 ± 88 | 860 ± 72 | 960 ± 84 | 810 ± 26 |
| | posterior left WM (blue) | 860 ± 70. | 850 ± 61 | 880 ± 79 | 820 ± 37 |
| | anterior GM (cyan) | 1200 ± 210 | 1200 ± 230 | 1300 ± 230 | 1300 ± 180 |
| $\hat{T}_2^{\mathrm{ML}}$ | anterior right WM (yellow) | 40. ± 1.3 | 54 ± 3.8 | 46 ± 1.5 | 55 ± 1.9 |
| | anterior left WM (magenta) | 40. ± 1.7 | 50. ± 4.5 | 44 ± 1.7 | 53 ± 1.8 |
| | posterior right WM (green) | 43 ± 2.7 | 60. ± 6.9 | 51 ± 3.6 | 59 ± 2.1 |
| | posterior left WM (blue) | 43 ± 1.8 | 57 ± 4.9 | 49 ± 2.5 | 57 ± 1.8 |
| | anterior GM (cyan) | 50 ± 12 | 60 ± 15 | 60 ± 11 | 59 ± 6.0 |